CrossMark

Human swallowing simulation based on videofluorography images using Hamiltonian MPS method

Takahiro Kikuchi[1] · Yukihiro Michiwaki[1] · Tetsu Kamiya[2] · Yoshio Toyama[2] ·
Tasuku Tamai[3] · Seiichi Koshizuka[3]

Abstract In developed nations, swallowing disorders and aspiration pneumonia have become serious problems. We developed a method to simulate the behavior of the organs involved in swallowing to clarify the mechanisms of swallowing and aspiration. The shape model is based on anatomically realistic geometry, and the motion model utilizes forced displacements based on realistic dynamic images to reflect the mechanisms of human swallowing. The soft tissue organs are modeled as nonlinear elastic material using the Hamiltonian MPS method. This method allows for stable simulation of the complex swallowing movement. A penalty method using metaballs is employed to simulate contact between organ walls and smooth sliding along the walls. We performed four numerical simulations under different analysis conditions to represent four cases of swallowing, including a healthy volunteer and a patient with a swallowing disorder. The simulation results were compared to examine the epiglottic downfolding mechanism, which strongly influences the risk of aspiration.

Keywords Swallowing · Particle method · Hamiltonian MPS method · Contact · Soft tissue · Epiglottis

✉ Takahiro Kikuchi
oralsurg@musashino.jrc.or.jp

1 Oral Surgery Division, Japanese Red Cross Musashino Hospital, 1-26-1, Kyonancho, Musashino, Tokyo 180-8610, Japan

2 R&D Division, Meiji Co., Ltd., 540, Naruda, Odawara, Kanagawa 250-0862, Japan

3 Graduate School of Engineering, The University of Tokyo, 7-3-1, Hongo, Bunkyo, Tokyo 113-8656, Japan

1 Introduction

Aspiration is the accidental entry of a food bolus into the trachea when swallowing. Aspiration may cause aspiration pneumonia, which has become a serious problem for the aging population of the developed world [28,29,47]. Pneumonia is often fatal in the elderly, and patients diagnosed with aspiration pneumonia are often limited in the variety of foods that they may ingest and thus experience a reduced quality of life.

Many methods for observing swallowing motions have been developed, including videofluorography (VF) [6,8,27,50], computed tomography (CT) [16,17,40], and magnetic resonance imaging (MRI) [13,33]. However, the temporal and spatial resolutions of the dynamic images obtained using these methods are not sufficient to understand the movements of the organs involved in swallowing and the food bolus in detail. In addition, the images obtained using these methods do not allow hypothesized swallowing mechanisms to be validated from a mechanical point of view. Therefore, many important aspects of swallowing remain to be explained and understood.

Numerical simulations have been applied in various fields of biomedical engineering [15,19,31,34,36]. The oral cavity and pharynx have been modeled in several simulations carried out to study speech and sleep apnea [2,5,9,14,35,37,43]. Numerical simulations of swallowing are valuable for representing the detailed movements of the organs involved in swallowing and the food bolus and in clarifying the mechanisms of swallowing and aspiration. Numerical simulations of swallowing can also be used as a predictive tool for estimating the risk of aspiration.

The numerical simulation of the food bolus flow during swallowing is difficult because it is a free surface flow involving splashing, separation, and reattachment. Sonomura et al.

[41] applied the arbitrary Lagrangian and Eulerian (ALE) method to simulate the movement of a food bolus flow, but small splashes were not represented. Particle methods such as smoothed particle hydrodynamics (SPH) and moving particle simulation (MPS) have also been applied [12,18,20] and found to be more useful. These particle methods can analyze such flows without any complex treatment [15,24].

The numerical simulation of organ movements is difficult because of the complex shapes and large deformations involved. Mizunuma et al. [30] presented a simulation of the oral cavity, pharynx, esophagus, and larynx. However, the shape and motion models that they used were overly simplified and not smooth because of problems with the calculation stability. Tsou et al. [48,49] used ArtiSynth, which is an open-source three-dimensional biomechanical simulation platform [7,42], to developed a three-dimensional model of the hyoid bone, larynx, and trachea with their associated muscles. They performed an inverse problem simulation of the hyolaryngeal elevation and anterior movement based on VF images to study the functions of each muscle. The hyolaryngeal excursion is important in epiglottic downfolding and esophageal opening. In their study, Tsou et al. omitted other organs, such as the tongue and epiglottis, and the food bolus. Ho et al. [11] performed a structural analysis of the tongue, palate, and oropharynx using ArtiSynth and then simulated the food bolus movement by the SPH method using the simulation results for organ surfaces as the wall boundary condition. The shapes of the oral cavity and oropharynx were modeled based on anatomical geometry, but the larynx and esophagus were omitted to demonstrate the applicability of the particle method to representing the food bolus flow. The organ motion model used by Ho et al. was not based on realistic timings or trajectories of any medical images. In the above studies, no simulation models were developed for the esophagus and larynx based on anatomically realistic geometry and realistic dynamic images.

In this study, we analyzed the behavior of the tongue, palate, pharynx, esophagus, and larynx based on CT and VF images with the aim of developing a simulation method for swallowing and clarifying the mechanisms of swallowing and aspiration. The Hamiltonian MPS (HMPS) method [23,44] was employed for the structural analysis of these organs. Kikuchi et al. [22] verified the applicability of this method to a hyperelastic material under large deformation, and they proposed a wall boundary condition for the method. Particle methods do not require the generation of a complex mesh and are useful for analyzing large deformations [19]. Additionally, organ analyses using particle methods can be suitably coupled with fluid analyses of food bolus flows because of the development of a fluid–structure coupling scheme [39].

In this study, we modeled several cases of swallowing movements, including that of a swallowing disorder, by conducting numerical simulations under four conditions. We compared the simulation results to examine the mechanism of epiglottic downfolding, which is one of the most important movements for preventing aspiration.

2 Particle method

2.1 Equations of motion and time integration scheme

In this study, the following equations involving the elastic, artificial potential, viscous, and contact forces were used:

$$\rho \frac{\partial \mathbf{v}}{\partial t} = \mathbf{f}_{\text{elastic}} + \mathbf{f}_{\text{artificial}} + \mathbf{f}_{\text{viscous}} + \mathbf{f}_{\text{contact}}, \tag{1}$$

where ρ and $\mathbf{v}$ denote the density and velocity, respectively. The organs are discretized into particles with initial diameters and masses of l_0 and m, respectively. Specific formulations of each force are described in Sects. 2.2, 2.4, 2.5 and 2.6, respectively.

In this study, the Euler symplectic time integration scheme was utilized. First, the intermediate momentum is calculated without considering any contact.

$$m_i \mathbf{v}_i^* = m_i \mathbf{v}_i^k + \frac{m_i}{\rho_i} \left(\mathbf{f}_{i,\text{elastic}}^k + \mathbf{f}_{i,\text{artificial}}^k + \mathbf{f}_{i,\text{viscous}}^k \right) \Delta t. \tag{2}$$

Next, contacts are detected, and the contact forces are computed. Finally, the momentum and position of particles are updated using the following formulas:

$$m_i \mathbf{v}_i^{k+1} = m_i \mathbf{v}_i^* + \frac{m_i}{\rho_i} \mathbf{f}_{i,\text{contact}}^* \Delta t, \tag{3}$$

$$\mathbf{x}_i^{k+1} = \mathbf{x}_i^k + \mathbf{v}_i^{k+1} \Delta t. \tag{4}$$

2.2 Hamiltonian MPS method

The elastic forces were calculated using the HMPS method [44].

The governing equations of elastodynamics are as follows:

$$\rho \frac{\partial \mathbf{v}}{\partial t} = -\frac{\partial W}{\partial \mathbf{r}}, \tag{5}$$

and

$$W = \mathbf{\Pi} : \mathbf{F}, \tag{6}$$

where W denotes the total elastic strain energy and $\mathbf{F}$ is the deformation gradient tensor. The first Piola–Kirchhoff stress tensor is given by the following equation:

$$\mathbf{\Pi} = \mathbf{FS}, \tag{7}$$

where $\mathbf{S}$ is the second Piola–Kirchhoff stress tensor.

Let $\mathbf{r}_{ij} = \mathbf{x}_j - \mathbf{x}_i$ and $\mathbf{r}_{ij}^0 = \mathbf{x}_j^0 - \mathbf{x}_i^0$ be the current and initial positions, respectively, of particle j relative to particle i. We defined the weight function as follows:

$$w_{ij}^0\left(|\mathbf{r}_{ij}^0|\right) = \begin{cases} \dfrac{r_{\text{e.elastic}}}{|\mathbf{r}_{ij}^0|} - 1, & \left(0 < |\mathbf{r}_{ij}^0| \leq r_{\text{e.elastic}}\right) \\ 0, & \left(r_{\text{e.elastic}} < |\mathbf{r}_{ij}^0|\right) \end{cases} \quad (8)$$

where $r_{\text{e.elastic}}$ is the effective radius. We used $r_{\text{e.elastic}} = 1.75l_0$.

In the HMPS method, the deformation gradient tensor $\mathbf{F}_i$ at the particle i is evaluated using the weighted least-squares method. The following error functional can be defined by using the weight function:

$$e_i(\mathbf{F}_i) = \sum_j |\mathbf{F}_i \mathbf{r}_{ij}^0 - \mathbf{r}_{ij}|^2 w_{ij}^0. \quad (9)$$

The functional minimum is given by

$$\frac{\partial e_i}{\partial \mathbf{F}_i} = 0, \quad (10)$$

which provides the following formula for the deformation gradient tensor $\mathbf{F}_i$:

$$\mathbf{F}_i = \left[\sum_j \mathbf{r}_{ij} \otimes \mathbf{r}_{ij}^0 w_{ij}^0\right] \mathbf{A}_i^{-1}, \quad (11)$$

where $\otimes$ denotes the tensor product and

$$\mathbf{A}_i = \sum_j \mathbf{r}_{ij}^0 \otimes \mathbf{r}_{ij}^0 w_{ij}^0. \quad (12)$$

From Eq. (5), we can obtain the elastic force as follows:

$$\mathbf{f}_{i,\text{elastic}} = \sum_j (\mathbf{F}_i \mathbf{S}_i \mathbf{A}_i^{-1} \mathbf{r}_{ij}^0 + \mathbf{F}_j \mathbf{S}_j \mathbf{A}_j^{-1} \mathbf{r}_{ij}^0) w_{ij}^0. \quad (13)$$

2.3 Constitutive laws

The second Piola–Kirchhoff stress tensor is given by the following equation:

$$\mathbf{S} = 2\frac{\partial W}{\partial \mathbf{C}}, \quad (14)$$

where $\mathbf{C} = \mathbf{F}^t\mathbf{F}$ denotes the right Cauchy–Green deformation tensor. In this study, the Mooney–Rivlin constitutive law was applied.

$$W = C_1^{\text{MR}}(\tilde{I}_1 - 3) + C_2^{\text{MR}}(\tilde{I}_2 - 3) + D_1(J - 1)^2, \quad (15)$$

where C_1^{MR}, C_2^{MR}, and D_1 are the material constants, J is the third invariant of $\mathbf{F}$, and the first and second reduced invariants of $\mathbf{C}$ are expressed by the following equations:

$$\tilde{I}_1 = J^{-2/3}I_1, \quad (16)$$
$$\tilde{I}_2 = J^{-4/3}I_2, \quad (17)$$

where I_1 and I_2 denote the invariants of $\mathbf{C}$. The zero-strain Young's modulus of the Mooney–Rivlin model is derived as follows:

$$E = 6\left(C_1^{\text{MR}} + C_2^{\text{MR}}\right). \quad (18)$$

2.4 Artificial potential forces

We employed the artificial potential forces developed by Kondo et al. [23]:

$$\begin{aligned} \mathbf{f}_{i,\text{artificial}} = \sum_j \Big(& C_i^{\text{art}}\left(\mathbf{r}_{ij} - \mathbf{F}_i\mathbf{r}_{ij}^0\right) \\ & + C_j^{\text{art}}\left(\mathbf{r}_{ij} - \mathbf{F}_j\mathbf{r}_{ij}^0\right) \Big) w_{ij}^0, \end{aligned} \quad (19)$$

where

$$C_i^{\text{art}} = \frac{\hat{E}_i d}{\sum_j |\mathbf{r}_{ij}^0|^2 w_{ij}^0}, \quad (20)$$

and d denotes the number of spatial dimensions. The coefficient $\hat{E}$ is a parameter for determining the amplitude of the forces that has the same dimensional units as the Young's modulus, but it has no physical meaning. We used the value of E calculated from Eq. (18) as $\hat{E}$.

When the deformation gradient tensor $\mathbf{F}_i$ is evaluated at the particles i, spurious singular modes and high-frequency local oscillations can occur [23]. The artificial force is applied as a stabilizer in the direction that cancels the error term of the weighted least-squares method given by Eq. (9) and suppresses the spurious singular modes and local oscillations [23].

2.5 Viscous force

To stabilize the calculation, we attenuated the particle velocity by using the following formula for the viscous forces associated with the standard MPS method [25]:

$$\mathbf{f}_{i,\text{viscous}} = \rho \nu \frac{2d}{\lambda n^0} \sum_j (\mathbf{v}_j - \mathbf{v}_i) w_{ij}^0, \quad (21)$$

where ν is the coefficient of the viscous force. We used $\nu = 2 \times 10^{-3}$ [m^2/s]. The coefficients λ and n^0 normalize the Laplacian model of the standard MPS method.

The HMPS method with the artificial potential force conserves the total energy; however, the addition of the viscous force decreases the energy.

2.6 Wall boundary condition

To analyze the contact between the organ walls and smooth sliding along the walls, we had to smooth the surfaces of the walls represented by particles. We also needed to consider the deformation of the elastic particles. To do so, we employed a penalty method that uses metaballs [22]. In this method, particle i, which is in contact with the wall of another organ, is accelerated by the following normal and friction forces:

$$\mathbf{f}_{i,\mathrm{nor}} = kp\mathbf{n}_m, \tag{22}$$

and

$$\mathbf{f}_{i,\mathrm{tan}} = \min\left(\rho_i \frac{|\mathbf{v}_{im,\mathrm{tan}}|}{\Delta t}, \mu_{\mathrm{tan}}|\mathbf{f}_{i,\mathrm{nor}}|\right) \frac{\mathbf{v}_{im,\mathrm{tan}}}{|\mathbf{v}_{im,\mathrm{tan}}|}, \tag{23}$$

respectively, where k, p, $\mathbf{n}_m$, and μ_{tan} denote the penalty coefficient, penetration, unit normal vector of the wall, and friction coefficient, respectively. Let $\mathbf{v}_{im}$ be the relative velocity between the particle i and the wall. The vector $\mathbf{v}_{im,\mathrm{tan}}$ is the component of $\mathbf{v}_{im}$ perpendicular to $\mathbf{n}_m$.

$$\mathbf{v}_{im,\mathrm{tan}} = \mathbf{v}_{im} - (\mathbf{v}_{im} \cdot \mathbf{n}_m)\mathbf{n}_m. \tag{24}$$

A higher value for the penalty coefficient is better as long as the analysis is stable because it means reduced penetration and increased accuracy for the analysis [51]. We used the following formula for the penalty coefficient:

$$k = \tilde{k}\frac{\rho}{\Delta t^2}, \tag{25}$$

where $\tilde{k} = 0.3$ denotes the spring ratio coefficient.

A particle that can contact the wall is referred to as a "slave," and the wall is the "master" (Fig. 1). In the following section, we explain the method used to determine the master surface based on the arrangement of master particles.
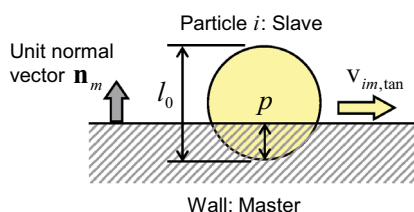

Fig. 1 Basic concept of penalty method

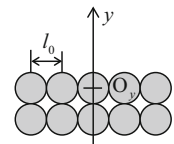**Fig. 2** Particle arrangement for calculation of $Z(y)$
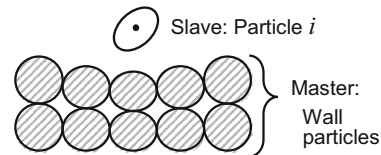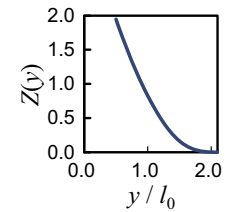

Fig. 3 Normal density function $Z(y)$

Fig. 4 Wall particles

2.7 Determination of master surface from master particles

A metaball method is employed to determine the master surface. This method is used to represent the surface of an object as a set of points [1] and to generate a surface from the simulation results using particle methods [10]. We used the following metaball function:

$$c(r) = \begin{cases} 1 - \left(\dfrac{r}{r_{\mathrm{e.metaball}}}\right)^2, & (0 < r \le r_{\mathrm{e.metaball}}) \\ 0, & (r_{\mathrm{e.metaball}} < r) \end{cases} \tag{26}$$

with the effective radius $r_{\mathrm{e.metaball}} = 1.75l_0$. Assuming a standard wall whose particles are arranged in a simple cubic lattice (Fig. 2), the relationship between the distance y and the summation of metaball functions can be defined as the normal density function $Z(y)$ (Fig. 3).

$$Z(y) = \sum_{j\in\mathrm{StandardWall}} c(|\mathbf{r}_{yj}|). \tag{27}$$

We next describe how to determine the position and normal direction of the master surface when the master particles are arranged as shown in Fig. 4. First, the summation of metaball functions from the master particles to the center of the slave particle i is calculated as follows:

$$C_{im} = \sum_{j\in\mathrm{master}} c\left(|\mathbf{F}_j^{-1}\mathbf{r}_{ij}|\right). \tag{28}$$
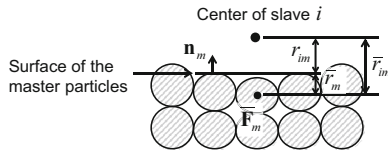
Fig. 5 Distance between slave particle i and master surface

Next, R_{im} is calculated from the inverse of the normal density function.

$$R_{im} = Z^{-1}(C_{im}). \tag{29}$$

R_{im} indicates how far the slave particle i is from the master surface without considering the deformation of the master particles. The unit normal vector of the master wall $\mathbf{n}_m$ and the velocity of the master wall $\mathbf{v}_{im}$ relative to the slave particle i are calculated as follows:

$$\mathbf{n}_m = -\frac{\sum\limits_{j \in \text{master}} \nabla c\left(|\mathbf{F}_j^{-1}\mathbf{r}_{ij}|\right)}{\left|\sum\limits_{j \in \text{master}} \nabla c\left(|\mathbf{F}_j^{-1}\mathbf{r}_{ij}|\right)\right|}, \tag{30}$$

$$\mathbf{v}_{im} = \frac{\sum\limits_{j \in \text{master}} (\mathbf{v}_j - \mathbf{v}_i)c\left(|\mathbf{F}_j^{-1}\mathbf{r}_{ij}|\right)}{C_{im}}. \tag{31}$$

Finally, the average strain of the master particles $\bar{\varepsilon}_m$ and the distance $\bar{r}_m$, as illustrated in Fig. 5, are calculated as follows:

$$\bar{\varepsilon}_m = \frac{1}{\left|\overline{\mathbf{F}}_m^{-1}\mathbf{n}_m\right|}, \tag{32}$$

$$\overline{\mathbf{F}}_m^{-1} = \frac{\sum\limits_{j \in \text{master}} c\left(|\mathbf{F}_j^{-1}\mathbf{r}_{ij}|\right)\mathbf{F}_j^{-1}}{C_{im}}, \tag{33}$$

$$\bar{r}_m = \bar{\varepsilon}_m l_0/2. \tag{34}$$

The indicator R_{im} is modified by $\bar{\varepsilon}_m$, and $\bar{r}_{im}$ is obtained.

$$\bar{r}_{im} = \bar{\varepsilon}_m R_{im}. \tag{35}$$

The distance between the center of the slave particle i and the master surface r_{im} is derived as follows:

$$r_{im} = \bar{r}_{im} - \bar{r}_m. \tag{36}$$

2.8 Penetration of a slave particle

We next describe how to compute the penetration of the slave particle i into the master surface while considering the deformation of the particle i. We can define the master surface
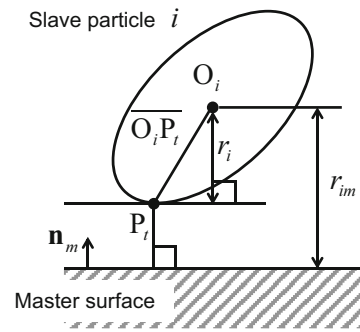

Fig. 6 Penetration between slave particle i and master surface

whose distance from the center of the slave particle i is r_{im} with the unit normal vector $\mathbf{n}_m$, as illustrated in Fig. 6. The slave particle i can be treated as a spheroid with the center $O_i = (0, 0, 0)$. The surface $P = (x, y, z)$ of the spheroid i can be represented as follows:

$$a_1 x^2 + a_2 y^2 + a_3 z^2 + a_4 xy + a_5 yz + a_6 zx = r_0^2, \tag{37}$$

where the constants a_n are calculated from the inverse of the deformation gradient tensor $\mathbf{F}_i^{-1}$. Next, we can obtain the point P_t on the spheroid i whose unit normal vector is $-\mathbf{n}_m$, and the component of the segment $\overline{O_i P_t}$ parallel to $-\mathbf{n}_m$ is r_i. The penetration is computed as follows:

$$p = \begin{cases} r_i - r_{im}, & (r_i > r_{im}) \\ 0, & (r_i \leq r_{im}). \end{cases} \tag{38}$$

2.9 Contact forces applied to slave and master particles

If $p > 0$, the slave particle i is subject to the following normal and friction forces:

$$\mathbf{f}_{i,\text{nor}} = kp\mathbf{n}_m, \tag{39}$$

$$\mathbf{f}_{i,\text{tan}} = \min\left(\rho_i \frac{|\mathbf{v}_{im,\text{tan}}|}{\Delta t}, \mu_{\text{tan}}|\mathbf{f}_{i,\text{nor}|}\right) \frac{\mathbf{v}_{im,\text{tan}}}{|\mathbf{v}_{im,\text{tan}}|}. \tag{40}$$

The master particles l are subject to the following reaction forces.

$$\mathbf{f}_{l,\text{nor\_react}} = \sum_{i \in \text{slave}} \left[-\frac{c\left(|\mathbf{F}_l^{-1}\mathbf{r}_{il}|\right)}{\sum\limits_{j \in \text{master}} c(|\mathbf{F}_j^{-1}\mathbf{r}_{ij}|)} \mathbf{f}_{i,\text{nor}} \right], \tag{41}$$

$$\mathbf{f}_{l,\text{tan\_react}} = \sum_{i \in \text{slave}} \left[-\frac{c\left(|\mathbf{F}_l^{-1}\mathbf{r}_{il}|\right)}{\sum\limits_{j \in \text{master}} c\left(|\mathbf{F}_j^{-1}\mathbf{r}_{ij}|\right)} \mathbf{f}_{i,\text{tan}} \right]. \tag{42}$$

Symmetrically treating all particles twice as both slaves and masters improves the reliability of the analysis, as

demonstrated in [3,45]. Therefore, we can use the summation of Eqs. (39), (40), (41) and (42) to represent the contact force used in Eq. (1).

$$\mathbf{f}_{i,\text{contact}} = \mathbf{f}_{i,\text{nor}} + \mathbf{f}_{i,\text{tan}} + \mathbf{f}_{i,\text{nor\_react}} + \mathbf{f}_{i,\text{tan\_react}}. \tag{43}$$

3 Shape and motion model of organs

3.1 Overview of modeling

This study was performed with the approval of the ethics committee of Japanese Red Cross Musashino Hospital. A CT image was taken using the normal procedure, and VF images were taken from a subject swallowing water mixed with an X-ray medium to obtain realistic geometry and motion data. A healthy 25-year-old volunteer was used as the subject of both the CT and VF images. VF is an observation method used to record dynamic images of swallowing using the X-ray fluoroscopic method.

The CT image provided three-dimensional surface data for the organs. Each organ was segmented manually because some organs were in contact when the CT image was taken. The surface data were transformed so that the angle of the neck and height of the larynx fit the rest position in the VF images. Additionally, the shapes of the tongue, soft palate, and esophagus were modified to reflect their initial shapes; their shapes when no forces are applied were assumed. The modified surface data were used to generate particles in a simple cubic lattice. The particle method used in this study permits the construction of shape data for analysis without the generation of a complex mesh. Figure 7 shows the shape model of the organs represented by particles.

Many types of muscles work together in various directions when a person swallows. Therefore, it is difficult to represent the organs' movements to fit realistic motion data by numerical simulation of the movements caused by muscle contraction. In this study, the swallowing movement was gen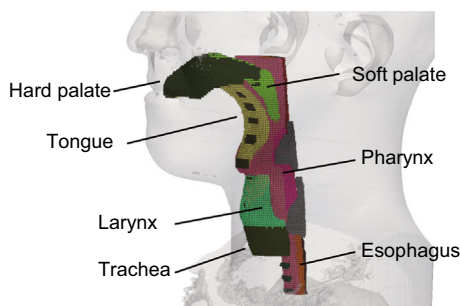erated using "control regions," which are defined as a group of particles that shift as a result of forced displacements. The time–displacement relationships of the control regions were determined on the basis of the VF images.

All of the particles were analyzed as a single continuous hyperelastic body. However, elastic analysis was not applied to the control regions of the pharyngeal constrictors, which are described in Sect. 3.6. Particles other than control regions were passively moved and deformed.

3.2 Tongue model

The tongue mainly consists of several types of muscles [21,46]. Based on this knowledge, Buchaillard et al. [2] developed a detailed simulation model for tongue muscles to represent tongue movement during speech. The tongue movement during swallowing seems to be like a traveling wave that transports a food bolus from the anterior to the posterior. This movement resembles those that occur when the genioglossus muscles contract from the anterior part to the posterior part, as shown by Buchaillard et al. [2]. A muscle itself is not able to make a pushing motion. However, the tongue is incompressible, so a decrease in one dimension will cause a compensatory increase in at least one other dimension [21]. Buchaillard et al. [2] showed that the contractions of the posterior part of the genioglossus muscle and styloglossus muscle elevate the surface of tongue toward the palate.

In this study, control regions were placed near the surface of the tongue to represent surface movement. A control region to sustain contact with the palate was established from the tip to the sides of the tongue (Fig. 8a). In addition, control regions were established from the tip to the base of the tongue on the midsagittal plane at certain intervals (Fig. 8b). The control regions were moved in the pull and push directions normal to the tongue surface in sequence from the anterior to the posterior in accordance with the VF images to represent the wave-like movement of the tongue. The inside part of the tongue was omitted from the shape model because the forced displacements were applied near the surface.
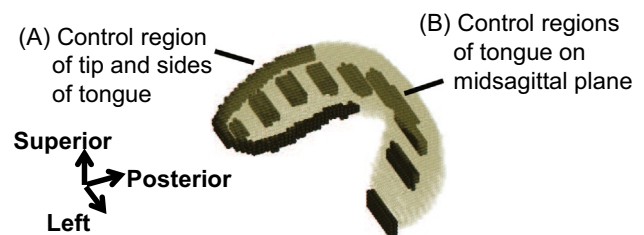

Fig. 7 Shape model of particles

Fig. 8 Tongue model (control regions are shown in back)

(F) Control region for central portion of the epiglottis

Elastic body : light green = Epiglottis, transparent green = other part of larynx

(E) Control region for thyroepiglottic ligament

(D) Control regions for arytenoid cartilages

(C) Control region for laryngeal and tracheal movement
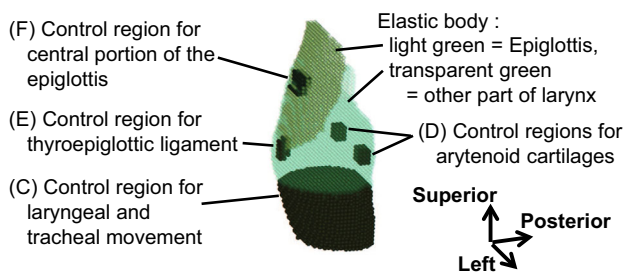
Superior
Posterior
Left

Fig. 9 Larynx and trachea model

3.3 Soft palate model

The soft palate is the organ that closes the flow channel from the oral cavity to the pharynx before swallowing and then closes the channel to the nasal cavity during swallowing. The former movement is mainly accomplished by the palatoglossus muscle, and the latter is mainly accomplished by the palatopharyngeal and levator veli palatini muscles.

To represent these movements, two control regions were established along the longitudinal axis on the midsagittal plane and moved toward the oral and nasal cavities.

3.4 Larynx and trachea model

The larynx is the entrance to the trachea. The larynx and the upper part of the trachea consist of the thyroid and cricoid cartilages. The cartilages are suspended from muscles and ligaments that hang down from the hyoid bone, so they move upward and forward together when the hyoid bone elevates and moves forward.

To represent the laryngeal and tracheal movement, a tube-shaped control region with the same height as the cricoid cartilage was established (Fig. 9c) and moved upward and forward in accordance with the VF images. The hyoid bone and thyroid cartilage themselves are not the flow channels of the food bolus; therefore, they were not considered in this study.

The larynx has true and false vocal cords. In this study, to mimic their biomechanics, cube-shaped control regions were established at the arytenoid cartilages, which are located at the posterior ends of the vocal cords (Fig. 9d). These control regions were moved together with control region (C) for laryngeal movement and given additional movement to the inside and anterior to represent the closing and opening of the entrance of the trachea during swallowing.

3.5 Epiglottis model

The epiglottis is an organ located in the larynx that folds down and covers the entrance of the larynx to prevent penetration of a food bolus into the larynx. The epiglottic cartilage is an elastic cartilage, which is the most flexible type of cartilage. The lower end of the epiglottic cartilage is attached to the thyroid cartilage by the thyroepiglottic ligament. In this study, a control region was established at the lower end of the epiglottic cartilage as the ligament (Fig. 9e) and was moved together with control region (C) for laryngeal movement.

The mechanism of epiglottic downfolding (i.e., what forces cause the epiglottis to rotate and what part of the epiglottis is acted upon by these forces) has not been clarified. The following mechanisms of epiglottic downfolding have been proposed in previous studies [6,8,27,50].

(α) The upper part of the epiglottis is pushed by the retracting wall of the tongue base.
(β) The upper part of the epiglottis is pushed by the constricting pharyngeal wall.
(γ) The lower part of the epiglottic cartilage is pressed by tissues next to the cartilage when the larynx elevates.
(δ) The muscles attached to the sides of the epiglottis pull downward.
(ϵ) The pressure of the food bolus produces a downward force.

The center of the epiglottic cartilage is also attached to the hyoid bone by the hyoepiglottic ligament. Because the position and shape of the epiglottis could not be seen clearly in the VF images and because the downfolding mechanism has not been clarified, the following two motion models about the center of epiglottic cartilage were constructed.

Model X: The center of the epiglottic cartilage is a control region (Fig. 9f) and given translational and rotational movements in accordance with the VF images (when an image was unclear, some presumptions were made based on the images captured before and afterward). The epiglottis is thus given active rotation by the control region and passive rotation by contact with other organs.

Model Y: The center of the epiglottic cartilage is not a control region and moves passively. The epiglottis is thus given only passive rotation by contact with other organs.

Active rotation of control region (F) in Model X represents the γ and δ mechanisms. Passive rotation by contact with other organs in Models X and Y corresponds to the α and β mechanisms. In this study, the γ and δ mechanisms could not be analyzed separately, and the food bolus (ϵ) was not considered. These issues will be examined in future research.

The simulation results obtained with Models X and Y were compared to investigate which of the four mechanisms (α–δ) occurs and when.

3.6 Pharynx model

The pharynx is the organ that connects the esophagus and larynx to the oral cavity and closes quickly to transport the food bolus to the esophagus during swallowing. The pharyngeal muscles consist of two groups: the muscles in the vertical direction, such as the palatopharyngeal muscle, and the constrictor muscles in the circular direction relative to the pharyngeal wall. These muscles constrict the pharynx transversely and shorten it vertically. However, this movement has not been quantitatively investigated in three dimensions.

In this study, a sheet-shaped surface with a thickness of approximately 4 mm was made by broadening the mucous surface obtained from the CT image and was used as the shape model for the pharyngeal wall. This model is illustrated in Fig. 10.

The control region of the cervical vertebrae for anchoring was established behind the posterior wall of the pharynx (Fig. 10g). Because muscle contraction was omitted and the only forced displacement is applied by the control regions, the vertical shortening of the posterior half of pharyngeal wall is not represented. The vertical shortening of the anterior half of the pharyngeal wall is passively represented by the laryngeal elevation of the control region (C).

To represent the transverse constriction of the pharynx, plate-like control regions (Fig. 10h) were established outside the shape model of the pharyngeal wall in consideration of the arrangement of the middle and inferior constrictors. The pharyngeal wall is subject to contact forces and is pushed inward by these control regions moving inward, as illustrated in Fig. 11.
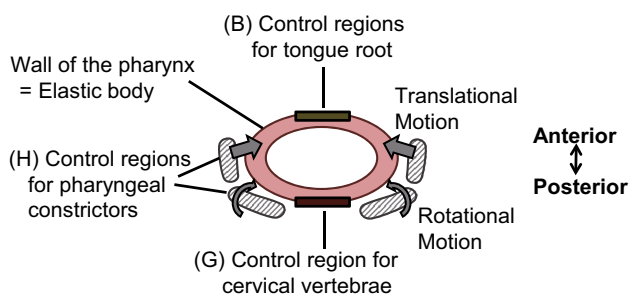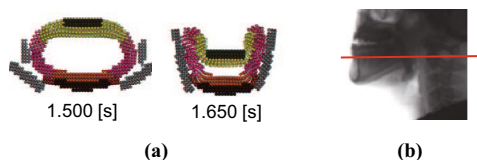

Fig. 10 Pharynx model

Fig. 11 Transverse constriction. **a** Sectional view. **b** Position of section

In this study, structures outside the sheet-like shape model for the pharyngeal wall, such as the sides and back of the neck, were omitted. This is because MRI images have indicated that the tissue near the pharynx seems to slide relative to the outer tissue near the surface of the neck when the larynx and pharynx move vertically during swallowing. Thus, the effects of external structures on the pharyngeal model were thought to be sufficiently small that they can be neglected.

3.7 Young's modulus and constitutive law

One of the most difficult problems in biomechanics is determining the physical properties of living organs. For ethical reasons, our ability to measure the physical parameters of living organs is limited, and few studies on this subject have been conducted. Furthermore, any such measurements obtained could vary widely because it is difficult to ensure uniformity in the specimens and measurement environment.

Some measurements of the Young's modulus of soft tissues such as the tongue have been reported. Gerard et al. [9] measured the stress–strain curve of a tongue removed from a fresh cadaver by indentation experiments and found its zero-strain Young's modulus to be 1.15 kPa. Cheng et al. [4] conducted MR elastography in vivo and reported a shear modulus of 2.67 kPa for tongue tissue and 2.53 kPa for soft palate tissue. Krouskop et al. [26] measured the Young's modulus of soft tissues in the forearm and leg *in vivo* using a gated Doppler ultrasonic system and reported a value of 6.2 kPa for the measured muscles at rest and 110 kPa for the muscles in contraction.

Various Young's modulus values have been used for soft tissues in previous simulation studies. Mizunuma et al. [30] simulated a swallowing movement using Young's moduli of 10 kPa for the tongue and 720 kPa for the pharynx. Dan et al. [5] simulated tongue movements during speech using a Young's modulus of 20 kPa for the tongue. In an analysis of the air flow and structure of the pharynx and larynx, Huang et al. [14] used a value of 6 kPa for the Young's modulus of the tongue based on the results reported by Krouskop et al. [26]. Buchaillard et al. [2] simulated the tongue during speech by modeling the tongue as a hyperelastic material according to the Yeoh model with a zero-strain Young's modulus of 6 kPa.

Few mentions of the Young's modulus of the epiglottis can be found in the literature. Huang et al. [14] used a Young's modulus of 1.6 MPa for the epiglottis in their simulation study. Pelteret et al. [35] numericallly simulated the tongue and surrounding tissues during breathing using a Young's modulus of 3 MPa for the epiglottis, but this was a measured value for the articular cartilage of human limbs, and the stiffness of the epiglottis is lower than that of articular cartilage.

Naumann et al. [32] measured the Young's modulus of the epiglottis in rabbits and reported a value of 0.24 MPa. In a study on the volume change of the ear canal, Qi et al. [36] simulated the elastic cartilage of a newborn using a Young's modulus of 30–90 kPa.

In this study, soft tissues such as the tongue, soft palate, pharynx, esophagus, and larynx were assigned a zero-strain Young's modulus value of 20 kPa. This value is the same as that used by Dan et al. [5] and lies between the values for muscles at rest and in contraction. During human swallowing, the Young's modulus may increase because of muscle contraction. However, the possible change in the Young's modulus was not considered in this study because muscle contractions were omitted, and the only forced displacement was applied by the control regions. The epiglottis was assigned a Young's modulus values of 100 kPa, i.e., five times greater than that assigned to the soft tissues. This value may also be smaller than the actual value. However, a smaller Young's modulus value for the epiglottis, which is affected by tongue and pharynx movements, will still represent the movement of the epiglottis and other organs appropriately.

The soft tissues are often treated as incompressible materials. Therefore, to prevent volume changes, we used the Mooney–Rivlin model given by Eq. (15) as the constitutive model rather than a linear elastic model and assigned a bulk modulus D_1 of 1 MPa. The ratio of $C_1^{MR}/C_2^{MR} = 1$ is widely used for soft tissues [36]. We applied this ratio and determined the values of C_1^{MR} and C_2^{MR} from the Young's modulus using Eq. (18).

3.8 Other parameters and conditions of analysis

Values of 1.0×10^{-5} [s] and 1.2×10^{-3} [m] were used for the time interval Δt and initial particle diameter l_0, respectively. The control regions had 25,536 particles, and the parts excluding the control regions had 50,008 particles. The density ρ was 1×10^3 [kg/m^3]. From the start of the analysis to 0.5 s later, the control regions were moved to deform the organ model to conform to the shape of the VF image before swallowing. Then, the swallowing movement was represented based on the VF images.

To our knowledge, the friction coefficients of the surfaces of the organs involved in swallowing have not been investigated. These friction coefficients are considered to be strongly related to the degree of drying of the oral cavity and pharynx. For example, the elderly have little saliva, so these organ walls become dry, and the friction coefficients may become large. In this study, two friction coefficient values of $\nu_{tan} = 0.1$ and 0.3 were used to investigate the sensitivity. As described in Sect. 3.5, two motion models for the epiglottis were constructed. Therefore, four cases were considered for numerical simulation, as indicated in table 1.

Table 1 Four cases for numerical simulation

Simulation case	Epiglottic motion	μ_{tan}
Case X1	Model X	0.1
Case X3	Model X	0.3
Case Y1	Model Y	0.1
Case Y3	Model Y	0.3

4 Results and discussions

4.1 Simulation results of basic case

In this section, we present the results for Case X1 as the basic case; it was most consistent with the VF images among the four simulation cases. Figure 12 shows the VF images, and Fig. 13 shows the corresponding snapshots for Case X1 illustrating only the right half of the organs' particles. Control region (H) for the pharyngeal constrictors is shown in gray, and the other control regions are shown in black. In Fig. 14, the epiglottis for Case X1 is shown from the left-rear point of view without the posterior wall of the pharynx.

The entire swallowing movement of the organs was stably analyzed using the HMPS method with the application of artificial potential forces and viscous forces. Each part of the organ model was deformed non-uniformly because each control region moved various distances in different directions. The entrance of esophagus opened considerably, as indicated in Fig. 13e, and elongated to more than twice its length in the anterior–posterior direction because of the laryngeal movement toward the anterior. For the particles outside the control regions, at time = 1.667 s, the average value of det **F** was 0.9992, and 98.0% of the particles maintained their det **F** within 0.98–1.02. These results indicate that the organ model behaved as an almost incompressible body, which reflected the effect of using the Mooney–Rivlin model.

In this study, the movements of the control regions were defined to correspond to the VF images. Therefore, the timings and displacements of the organs' movements were consistent with the realistic swallowing of the human volunteer in this study. In addition, the tip of the epiglottis, which was not a control region, passively moved and successfully folded down below the horizontal. The epiglottic tip rotated beyond the angle of control region (F) because it was pushed by the pharyngeal wall when control region (H) for the pharyngeal constrictors moved, as indicated in Fig. 14. The epiglottis slid smoothly along the pharyngeal wall and rotated below the horizontal. No differences were observed between the VF images and the simulation results for the movement of the epiglottic tip.
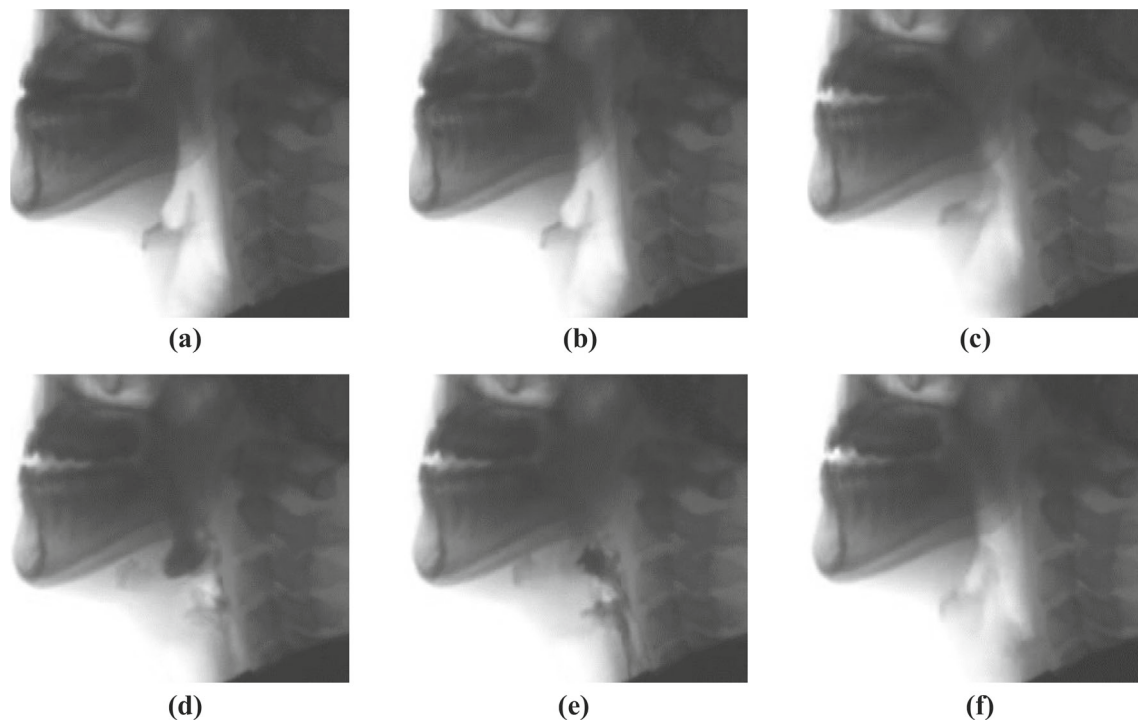
Fig. 12 Lateral view of VF images. **a** 0.000 [s]. **b** 0.500 [s]. **c** 1.383 [s]. **d** 1.583 [s]. **e** 1.667 [s]. **f** 2.050 [s]

4.2 Comparison of four cases to clarify epiglottic downfolding mechanism

Figures 15 and 16 shows the results for Cases Y1 and Y3, respectively. Table 2 lists the times at which the tip of the epiglottis rotated below the horizontal for the four cases. In Cases X1 and X3, where control region (F) was established, the epiglottis rotated below the horizontal, but the higher friction coefficient resulted in later epiglottic downfolding because of the friction force applied by the pharyngeal wall. In Cases Y1 and Y3, where the center of the epiglottic cartilage was not actively moved, the upper part of the epiglottis contacted a larger area than in Cases X1 and X3 for the time interval of 1.63–1.69 s. Subsequently, the lower friction coefficient caused the epiglottis to slide on the posterior pharyngeal wall and fold below the horizontal (Fig. 15d). With a higher friction coefficient, on the other hand, the epiglottis was prevented from rotating by contact with the pharyngeal wall (Fig. 16) and did not fold down until the end of swallowing.

Figure 17 compares the VF image and the results for Cases X1 and Y1 at the time = 1.700 s. The red sectional outline corresponds to the epiglottis for Case X1, and the yellow outline corresponds to the epiglottis for Case Y1. The height of the epiglottis for Case Y1 was lower than that for Case X1 and was not consistent with the location of the shadow of the food bolus, which is visible in the VF image. Therefore, the epiglottis in this VF image was considered to bend while keeping its center part high, which corresponds to the shape obtained for Case X1 when its position was below the horizontal.

We next discuss the epiglottic downfolding mechanisms α–δ, which are explained in Sect. 3.5. In Cases X1 and X3, the epiglottis rotated to a position slightly above the horizontal because of the action of control region (F), which corresponded to the model for laryngeal elevation (γ) and epiglottic muscles (δ). The epiglottis was then rotated passively below the horizontal by the pharyngeal push (β) from the lateral–posterior direction. The results for Case X1 and X3 suggest that the wall of the tongue base (α) may not have worked to produce epiglottic downfolding as the volunteer swallowed.

In Case Y1, the epiglottis was pushed backward by the wall of the tongue base (α) rather than control region (F) (γ, δ) and was then rotated below the horizontal by the pharyngeal push (β). Logemann et al. [26] hypothesized that epiglottic downfolding from the horizontal position to below the horizontal is caused by the epiglottis being crushed between the retracting wall of the tongue base and the constricting pharyngeal wall. The downfolding mechanism described by their hypothesis was considered to be almost the same as that represented by Case Y1. However, there is a small difference. According to the hypothesis presented by Logemann et al., the midsagittal part of the pharyngeal wall pushes the epiglottis. In our analysis, the relatively lateral part of the posterior pharyngeal wall pushed the epiglottis.
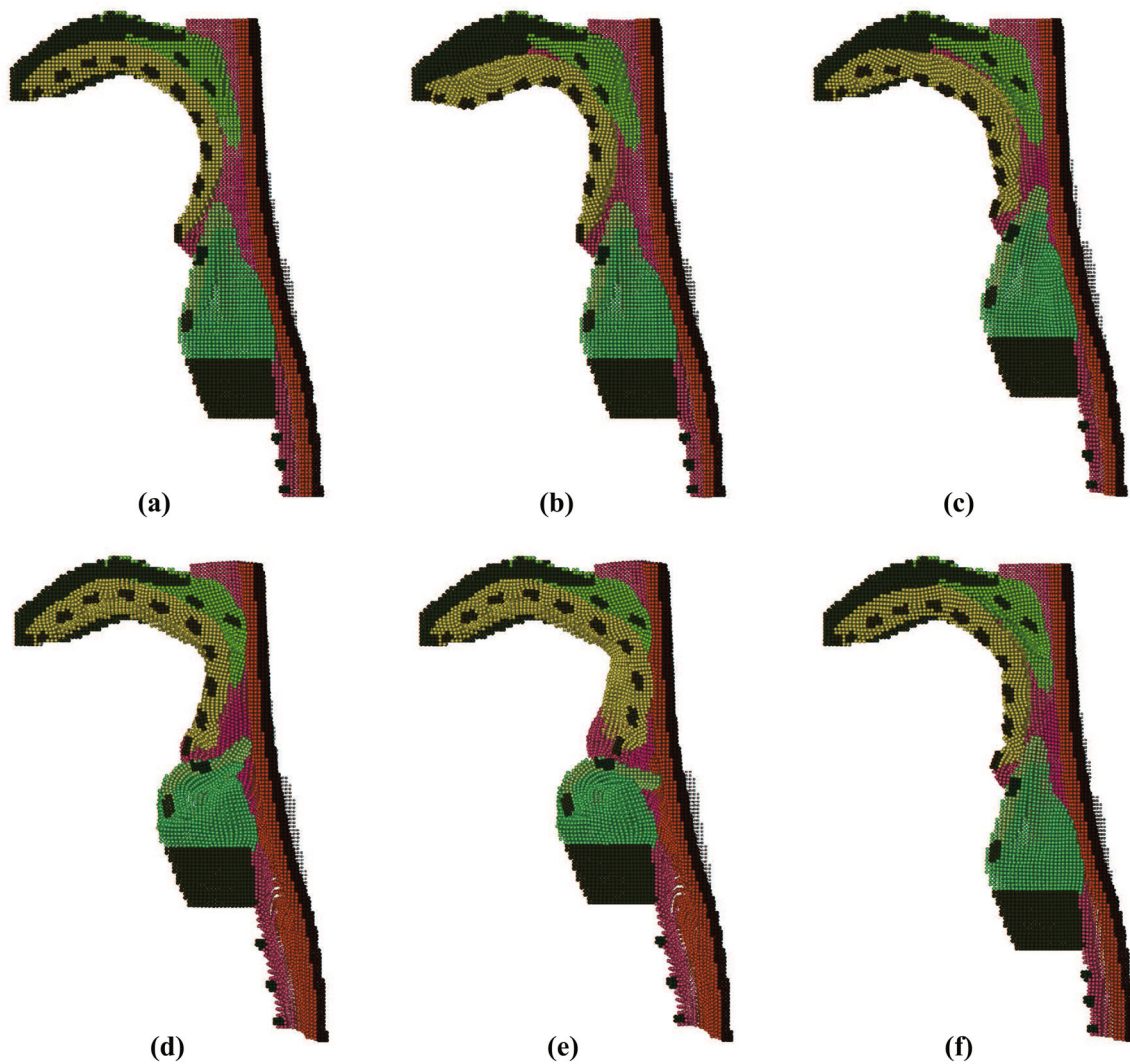
Fig. 13 Lateral view of basic case. **a** 0.000 [s]. **b** 0.500 [s]. **c** 1.383 [s]. **d** 1.583 [s]. **e** 1.667 [s]. **f** 2.050 [s]

The results for Case Y1 suggest that the retraction of the wall of the tongue base (α) is important in epiglottic downfolding when the epiglottic rotations caused by the laryngeal elevation (γ) and epiglottic muscles (δ) (control region (F)) are absent because of some disorder.

Finally, we discuss factors that prevent epiglottic downfolding. Even if some forces that tend to make the epiglottis rotate are applied, a large area of contact between the epiglottis and the posterior pharyngeal wall prevents the epiglottis from folding down. When the epiglottis was folding down and approximately at the horizontal position, epiglottic contact with the pharyngeal wall was observed in many cases in the VF images, including those obtained for the volunteer in this study. However, the size of the contact area varied from case to case. In Cases Y1 and Y3, the epiglottis was largely in contact with the pharyngeal wall, as indicated in Figs. 15c and 16, and was similar to that of a patient with a swallowing

disorder, as indicated in Fig. 18. Despite the same motion model being applied, the epiglottis folded below the horizontal in Case Y1 but did not in Case Y3. If the epiglottis does not rotate and does not cover the entrance to the larynx, the risk of aspiration becomes high. In this study, the friction coefficients were not validated in a quantitative manner, but the results qualitatively showed that the friction coefficient may be a factor that prevents epiglottic downfolding.

In addition, the comparison of Cases X1 and Y1 illustrated in Fig. 17 indicates that the anterior–superior movement of the center of the epiglottic cartilage in Case X1 and the VF image plays a role in making the tip of the epiglottis lose contact with the pharyngeal wall and rotate below the horizontal. Vandaele et al. [50] proposed that the anterior movement of the hyoid bone provides some traction to the center of the epiglottic cartilage via the hyoepiglottic ligament. In Model X, the translational movement of control
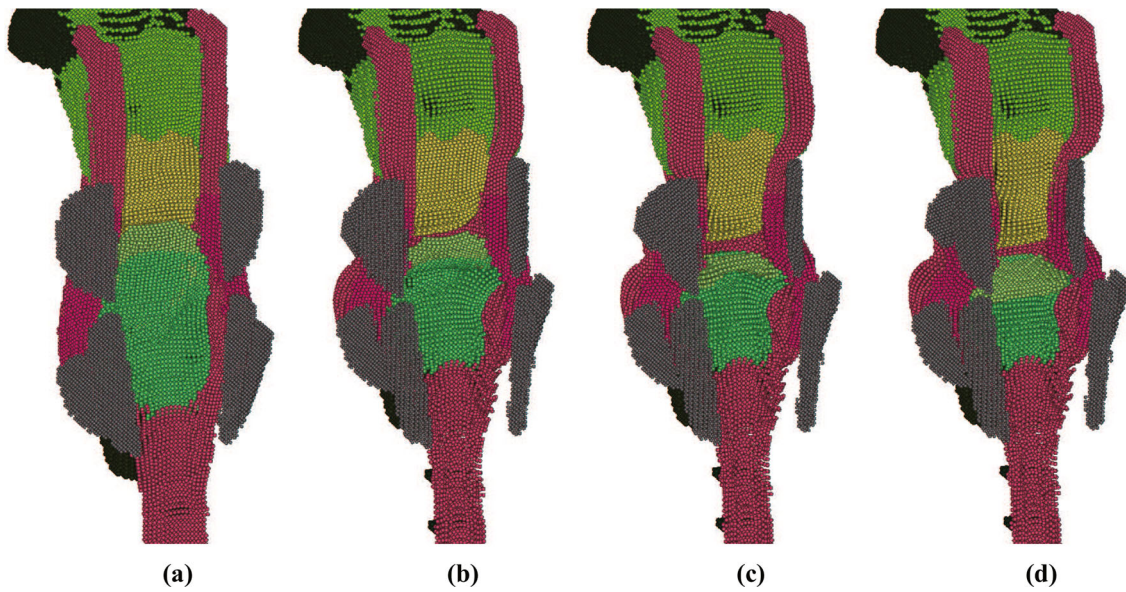
Fig. 14 Rear view of basic case. **a** 1.383 [s]. **b** 1.583 [s]. **c** 1.633 [s]. **d** 1.677 [s]

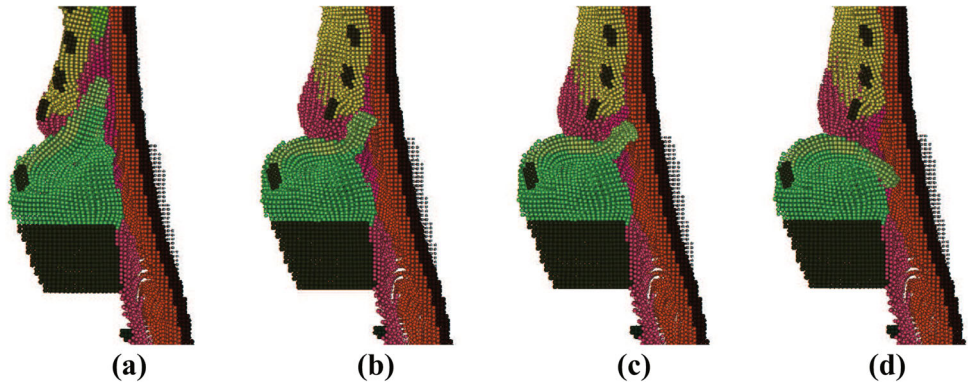**Fig. 15** Lateral view of Case Y1. **a** 1.583 [s]. **b** 1.677 [s]. **c** 1.683 [s]. **d** 1.700 [s]
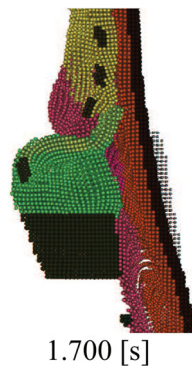

Fig. 16 Lateral view of case Y3

1.700 [s]

Table 2 Time of epiglottic downfolding below horizontal

Simulation case	Time [s]
Case X1	1.65
Case X3	1.70
Case Y1	1.70
Case Y3	Did not fold

region (F) corresponds to a motion model for the pulling of the hyoepiglottic ligament based on the VF images and some assumptions. On the other hand, because the center of the epiglottic cartilage in Model Y was not subjected to a forced translational movement, its movement corresponds to that of a patient for whom the hyoepiglottic ligament is weakened or the degree of hyoid movement toward the superior and anterior is small. The elderly have fewer fibers in the hyoepiglottic ligament [38]. The hyoepiglottic ligament may also loosen because the larynx position at rest becomes lower with age. Additionally, the degree of hyoid movement often decreases if a person's reflexes are damaged. In these cases, the anterior–superior movement of the center of the epiglottic cartilage may become less than normal, as represented in Cases Y1 and Y3, so the epiglottis will largely be in contact with the pharyngeal wall and have difficulty folding down below the horizontal. This results in a higher possibility of aspiration.
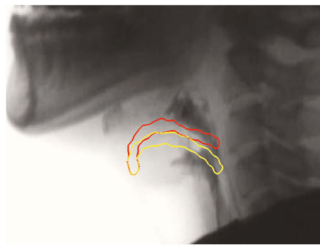
1.700 [s]

Fig. 17 Comparison of Cases X1 and Y1 with VF image (Case X1: *red*, Case Y1: *yellow*). (Color figure online)
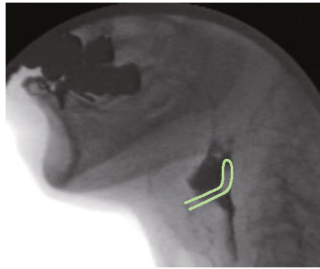

Fig. 18 VF image of patient for whom epiglottic downfolding is absent (Case Y3)

5 Conclusion

The swallowing movements of the tongue, palate, pharynx, esophagus, and larynx were successfully analyzed. A shape model was constructed on the basis of the anatomical geometry. A motion model that utilizes the forced displacements of control regions was constructed on the basis of realistic dynamic images to reflect the most current medical and medical engineering knowledge on the mechanisms of human swallowing. The HMPS method was used with the application of artificial potential and viscous forces for stable analysis of the organ movements. The epiglottis slides smoothly on the pharyngeal wall and folds down below the horizontal given the wall boundary conditions applied by the penalty method using metaballs.

We ran four numerical simulations with different motion models of the epiglottis or friction coefficients to represent four cases of swallowing, including a swallowing disorder. We compared the simulation results with VF images and analyzed the factors that contribute to or prevent the folding down of the epiglottis. The simulation results yielded considerable insight into the causes of swallowing disorders and the mechanisms of epiglottic downfolding, which have a strong influence on the risk of aspiration.

In future research, we will simulate the flow of a food bolus using a coupling scheme that incorporates fluid analysis. The structural and fluid analyses will be validated through a comparison between the simulation results for the shape and movement of the food bolus with VF images. In addition, we will validate the relationship between the force applied to the epiglottis and its rotation angle by comparing the results of experiments and simulations.

References

1. Blinn JF (1982) A generalization of algebraic surface drawing. ACM Trans Graph 1(3):235–256. doi:10.1145/357306.357310
2. Buchaillard S, Perrier P, Payan Y (2009) A biomechanical model of cardinal vowel production: muscle activations and the impact of gravity on tongue positioning. J Acoust Soc Am 126(4):2033–2051. doi:10.1121/1.3204306
3. Campbell J, Vignjevic R, Libersky L (2000) A contact algorithm for smoothed particle hydrodynamics. Comput Meth Appl Mech Eng 184(1):49–65. doi:10.1016/S0045-7825(99)00442-9
4. Cheng S, Gandevia SC, Green M, Sinkus R, Bilston LE (2011) Viscoelastic properties of the tongue and soft palate using MR elastography. J Biomech 44(3):450–454. doi:10.1016/j.jbiomech.2010.09.027
5. Dang J, Honda K (2004) Construction and control of a physiological articulatory model. J Acoust Soc Am 115(2):853–870. doi:10.1121/1.1639325
6. Ekberg O, Sigurjonsson SV (1982) Movement of the epiglottis during deglutition: a cineradiographic study. Gastroint Radiol 7(1):101–107. doi:10.1007/BF01887619
7. Fels S, Gick B, Hannam A et al. (2014) ArtiSynth, 3D biomechanical modeling toolkit. http://www.magic.ubc.ca/artisynth/pmwiki.php. Accessed 18 Sept 2014
8. Fink BR, Martin RW, Rohrmann CA (1979) Biomechanics of the human epiglottis. Acta Otolaryngol 87(3–6):554–559. doi:10.3109/00016487909126464
9. Gerard JM, Ohayon J, Luboz V, Perrier P, Payan Y (2005) Nonlinear elastic properties of the lingual and facial tissues assessed by indentation technique: application to the biomechanics of speech production. Med Eng Phys 27(10):884–892. doi:10.1016/j.medengphy.2005.08.001
10. Goswami P, Schlegel P, Solenthaler B, Pajarola R (2010) Interactive SPH simulation and rendering on the GPU. Proceedings ACM SIGGRAPH/Eurographics symposium on computer animation, 55–64
11. Ho AK, Tsou L, Green S, Fels S (2014) A 3D swallowing simulation using smoothed particle hydrodynamics. Comput Meth Biomech Biomed Eng 2(4):237–244. doi:10.1080/21681163.2013.862862
12. Ho AK, Nicosia MA, Dietsch A, Pearson W, Rieger J, Solomon N, Stone M, Inamoto Y, Saitoh E, Green S, Fels S (2014) 3D dynamic visualization of swallowing from multi-slice computed tomography. SIGGRAPH Posters 2014:103. doi:10.1145/2614217.2633399
13. Honda Y, Hata N (2007) Dynamic imaging of swallowing in a seated position using open-configuration MRI. J Magn Reson Imaging 26(1):172–176. doi:10.1002/jmri.20992
14. Huang Y, Malhotra A, White DP (2005) Computational simulation of human upper airway collapse using a pressure-/state-dependent model of genioglossal muscle contraction under laminar flow conditions. J Appl Physiol 99(3):1138–1148. doi:10.1152/japplphysiol.00668.2004
15. Imai Y, Kobayashi I, Ishida S, Ishikawa T, Buist M, Yamaguchi T (2013) Antral recirculation in the stomach during gastric mixing. Am J Physiol Gastrointest Liver Physiol 304(5):G536–G542. doi:10.1152/ajpgi.00350.2012

16. Inamoto Y, Fujii N, Saitoh E, Baba M, Okada S, Katada K, Ozeki Y, Kanamori D, Palmer JB (2011) Evaluation of swallowing using 320-detector-row multislice CT. Part II: kinematic analysis of laryngeal closure during normal swallowing. Dysphagia 26(3):209–217. doi:10.1007/s00455-010-9276-2

17. Inamoto Y, Saitoh E, Okada S, Kagaya H, Shibata S, Ota K, Baba M, Fujii N, Katada K, Wattanapan P, Palmer JB (2013) The effect of bolus viscosity on laryngeal closure in swallowing: kinematic analysis using 320-row area detector CT. Dysphagia 28(1):33–42. doi:10.1007/s00455-012-9410-4

18. Ishida S, Imai Y, Ishikawa T, Kinjo A, Matsuki N (2011) Numerical simulation of swallowing based on videofluorography. 24th Jpn Soc Mech Eng Comput Mech Div Conf 2011:639–641 [in Japanese]

19. Ito H, Koshizuka S, Nakagawa K, Haga A (2010) Particle simulation of lung deformation in axial plane by chest respiration and heartbeat. Trans Jpn Soc Simul Technol 2(3):93–100. doi:10.11308/tjsst.2.93 [in Japanese]

20. Kamiya T, Toyama Y, Michiwaki Y, Kikuchi T (2013) Development of a numerical simulator of human swallowing using a particle method (Part 2. Evaluation of the accuracy of a swallowing simulation using the 3D MPS method). Conf Proc IEEE Eng Med Biol Soc 2013:2992–2995. doi:10.1109/EMBC.2013.6610169

21. Kier WM, Smith KK (1985) Tongues, tentacles and trunks: the biomechanics of movement in muscular-hydrostats. Zool J Linn Soc 83(4):307–324. doi:10.1111/j.1096-3642.1985.tb01178.x

22. Kikuchi T, Michiwaki Y, Koshizuka S, Kamiya T, Osada T, Jinno N, Toyama Y (2014) Simulation of uniaxial compression based on Hamiltonian MPS method with wall boundary condition using penalty method. Trans Jpn Soc Comput Eng Sci 2014:20140010. doi:10.11421/jsces.2014.20140010 [in Japanese]

23. Kondo M, Suzuki Y, Koshizuka S (2010) Suppressing local particle oscillations in the Hamiltonian particle method for elasticity. Int J Numer Meth Eng 81(12):1514–1528. doi:10.1002/nme.2744

24. Koshizuka S (2011) Current achievements and future perspectives on particle simulation technologies for fluid dynamics and heat transfer. J Nucl Sci Technol 48(2):155–168. doi:10.1080/18811248.2011.9711690

25. Koshizuka S, Oka Y (1996) Moving-particle semi-implicit method for fragmentation of incompressible fluid. Nucl Sci Eng 123(3):421–434

26. Krouskop TA, Dougherty DR, Vinson FS (1987) A pulsed doppler ultrasonic system for making noninvasive measurements of the mechanical properties of soft tissue. J Rehabil Res Dev 24(2):1–8

27. Logemann JA, Kahrilas PJ, Cheng J, Pauloski BR, Gibbons PJ, Rademaker AW, Lin S (1992) Closure mechanisms of laryngeal vestibule during swallow. Am J Physiol 262(2 Pt 1):G338–G344

28. Ministry of Health, Labour and Welfare, Japan (2012) Patient survey in Japan, 2011. http://www.mhlw.go.jp/toukei/saikin/hw/kanja/11/index.html. Accessed 18 Sept 2014 [in Japanese]

29. Ministry of Health, Labour and Welfare, Japan (2014) Vital statistics in Japan, 2013. http://www.mhlw.go.jp/toukei/saikin/hw/jinkou/kakutei13/index.html. Accessed 18 Sept 2014 [in Japanese]

30. Mizunuma H, Sonomura M, Shimokasa K, Ogoshi H, Nakamura S, Tayama N (2009) Numerical modeling and simulation on the swallowing of jelly. J Texture Stud 40(4):406–426. doi:10.1111/j.1745-4603.2009.00189.x

31. Nakamura Y, Yamane K, Fujita Y, Suzuki I (2005) Somatosensory computation for man-machine interface from motion-capture data and musculoskeletal human model. IEEE Trans on Robot 21(1):58–66. doi:10.1109/TRO.2004.833798

32. Naumann A, Dennis JE, Awadallah A, Carrino DA, Mansour JM, Kastenbauer E, Caplan AI (2002) Immunochemical and mechanical characterization of cartilage subtypes in rabbit. J Histochem Cytochem 50(8):1049–1058. doi:10.1177/002215540205000807

33. Olthoff A, Zhang S, Schweizer R, Frahm J (2014) On the physiology of normal swallowing as revealed by magnetic resonance imaging in real time. Gastroenterol Res Pract 2014:493174. doi:10.1155/2014/493174

34. Oshima M (2004) A new approach to cerebral hemodynamics: patient-specific modeling and numerical simulation of blood flow and arterial wall interaction. IACM Expr Bull Int Assoc Comput Mech 16:4–9

35. Pelteret JP, Reddy BD (2012) Computational model of soft tissues in the human upper airway. Int J Numer Meth Biomed Eng 28(1):111–132. doi:10.1002/cnm.1487

36. Qi L, Liu H, Lutfy J, Funnell WR, Daniel SJ (2006) A non-linear finite-element model of the newborn ear canal. J Acoust Soc Am 120(6):3789–3798. doi:10.1121/1.2363944

37. Rasani MR, Inthavong K, Tu JY (2011) Simulation of pharyngeal airway interaction with air flow using low-Re turbulence model. Modell Simul Eng 2011:510472. doi:10.1155/2011/510472

38. Sawatsubashi M, Umezaki T, Kusano K, Tokunaga O, Oda M, Komune S (2010) Age-related changes in the hyoepiglottic ligament: functional implications based on histopathologic study. Am J Otolaryngol 31(6):448–452. doi:10.1016/j.amjoto.2009.08.003

39. Shao Y, Yamakawa T, Kikuchi T, Shibata K, Koshizuka S (2013) A three-dimensional coupling method for fluid-structure interaction problems by using explicit MPS method and Hamiltonian MPS method. Trans Jpn Soc Comput Eng Sci 2013:20130004. doi:10.11421/jsces.2013.20130004 [in Japanese]

40. Shibata S, Kagaya H, Inamoto Y, Saitoh E, Okada S, Ota K, Kanamori D (2011) Swallowing maneuver analysis using 320-row area detector computed tomography (320-ADCT). Jpn J Compr Rehabil Sci 2:54–62. doi:10.11336/jjcrs.2.54

41. Sonomura M, Mizunuma H, Numamori T, Michiwaki Y, Nishinari K (2011) Numerical simulation of the swallowing of liquid bolus. J Texture Stud 42(3):203–211. doi:10.1111/j.1745-4603.2011.00287.x

42. Stavness I, Lloyd JE, Fels S (2012) Automatic prediction of tongue muscle activations using a finite element model. J Biomech 45(16):2841–2848. doi:10.1016/j.jbiomech.2012.08.031

43. Stavness I, Hannam AG, Lloyd JE, Fels S (2010) Predicting muscle patterns for hemimandibulectomy models. Comput Meth Biomech Biomed Eng 13(4):483–491. doi:10.1080/10255841003762034

44. Suzuki Y, Koshizuka S (2008) A Hamiltonian particle method for non-linear elastodynamics. Int J Numer Meth Eng 74(8):1344–1373. doi:10.1002/nme.2222

45. Swegle JW, Attaway SW, Heinstein MW, Mello FJ, Hicks DL (1994) An analysis of smoothed particle hydrodynamics. Sandia Report: SAND93-2513

46. Takemoto H (2001) Morphological analyses of the human tongue musculature for three-dimensional modeling. J Speech Lang Hear Res 44(1):95–107. doi:10.1044/1092-4388(2001/009)

47. Teramoto S, Fukuchi Y, Sasaki H, Sato K, Sekizawa K, Matsuse T (2008) High incidence of aspiration pneumonia in community- and hospital-acquired pneumonia in hospitalized patients: a multicenter, prospective study in Japan. J Am Geriatr Soc 56(3):577–579. doi:10.1111/j.1532-5415.2008.01597.x

48. Tsou L (2012) The effects of muscle aging on hyoid motion during swallowing: a study using a 3D biomechanical model. Master thesis, University of British Columbia

49. Tsou L, Fels S (2011) Biomechanical modeling of the external laryngeal structures. Int Symp on Speech Sci 2011:133–138

50. Vandaele DJ, Perlman AL, Cassell MD (1995) Intrinsic fibre architecture and attachments of the human epiglottis and their contributions to the mechanism of deglutition. J Anat 186(Pt 1):1–15

51. Wang J, Chan D (2014) Frictional contact algorithms in SPH for the simulation of soil-structure interaction. Int J Numer Anal Meth Geomech 38(7):747–770. doi:10.1002/nag.2233